J. Fluid Mech. (2021), *vol*. 912, A50, doi:10.1017/jfm.2020.1121

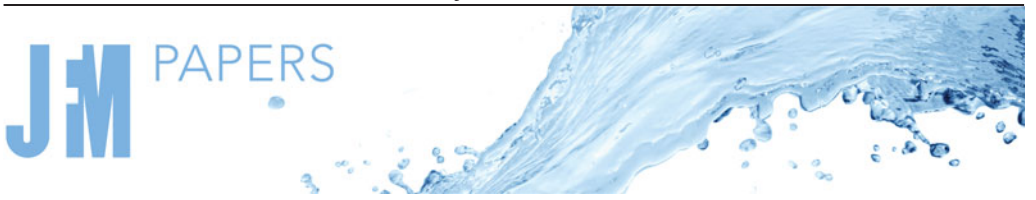

Experimental investigation of the acceleration statistics and added-mass force of deformable bubbles in intense turbulence

Ashwanth K.R. Salibindla[1], **Ashik Ullah Mohammad Masuk**[1] **and Rui Ni**[1],†

[1]Department of Mechanical Engineering, Johns Hopkins University, Baltimore, MD 21210, USA

(Received 8 May 2020; revised 23 November 2020; accepted 10 December 2020)

We present an experimental investigation of the acceleration statistics and the added mass tensor of deformable gas bubbles in turbulence. By simultaneously tracking both bubbles and their surrounding flow in three dimensions, we find two independent ways of estimating the bubble acceleration: either directly measured from three-dimensional bubble trajectories or indirectly calculated from the bubble's equation of motion. When such an equation is projected onto the bubble frame, the added-mass coefficient becomes a diagonal tensor with three elements being linked to the standard deviation of bubble acceleration along three bubble principal axes. This constraint aids in experimentally determining the added mass coefficient tensor. The obtained trend of C_A seems to agree with Lamb's potential flow solutions for spheroids, suggesting that the added-mass force on deformable bubbles can be modelled using spheroids with the same geometry and orientation. In addition, the probability density function of the relative orientation between the semi-major axis of deformed bubbles and the slip acceleration in turbulence is shown. A surprising finding is that the bubble orientation, indicated by the bubble's major axis, is not random in turbulence but rather is preferentially aligned with the slip acceleration. The degree of this alignment increases as bubbles deform more. Because accelerating along the major axis of a more deformed bubble entails reduced added mass, the acceleration standard deviation of deformable bubbles increases as a function of the bubble aspect ratio.

Key words: bubble dynamics, multiphase flow, isotropic turbulence

1. Introduction

From breaking waves (Deane & Stokes 2002) and free surface turbulence (Yu, Hendrickson & Yue 2020) to chemical and nuclear reactors (Michiyoshi & Serizawa 1986; Jakobsen 2008), two-phase flows consisting of finite-sized deformable bubbles or droplets

† Email address for correspondence: rui.ni@jhu.edu

are ubiquitous in nature and industrial applications. Their complicated interaction with the surrounding turbulent flows poses significant challenges to both numerical and experimental methods (Verschoof *et al.* 2016; Loisy & Naso 2017; Alméras *et al.* 2019; Du Cluzeau, Bois & Toutant 2019), as the interface deformation tends to modulate many hydrodynamic forces experienced by bubbles/droplets. In particular, it is well known that additional fluid forces tend to act upon an object as it accelerates relative to its surrounding flow; in turbulence, however, this relative acceleration between the two phases could originate either from the unsteady turbulent background flow or bubble/droplet deformation.

To understand the added-mass force, consider a case of fluid suddenly exerting force $\boldsymbol{F}$ on a neutrally buoyant object in translational motion without rotation (Batchelor 1967). By applying the potential flow theory, this force can be expressed as a function of the velocity potential (ϕ): $\boldsymbol{F} = -\rho_l \int (\partial\phi/\partial t)\hat{\boldsymbol{n}}\,\mathrm{d}A$, where ρ_l is the density of the ambient fluid. Since the velocity potential can be expressed as $\partial\phi/\partial t = \dot{\boldsymbol{u}}_s \cdot \boldsymbol{\Phi}$, this unsteady force can be written as $F_i = -\rho_l (a_s)_j \int \Phi_j n_i\,\mathrm{d}A$, where $\boldsymbol{\Phi}$ solely depends on the object's shape. Because the force F_i is linearly proportional to the object slip acceleration $(a_s)_j$ based on Newton's second law, the remaining coefficient ($\boldsymbol{A}_{ij} = \rho_l \int \Phi_j n_i\,\mathrm{d}A$) can be treated as an induced or virtual mass, which must be added to the real mass of the object when determining its response to a given applied force. The added-mass tensor $\boldsymbol{A}$ can be written as $\rho_l V_b \boldsymbol{C}_A$, where $\rho_l V_b$ is the mass of the object if filled with outside liquid with density ρ_l and $\boldsymbol{C}_A$ is the tensorial added-mass coefficient. In addition to the added mass in response to translational acceleration, the potential flow analysis can also be extended to describe an object's response to a sudden torque from the surrounding fluid. In this case, the virtual moment of inertia ($\boldsymbol{D}$) must be added to the object's own moment of inertia ($\boldsymbol{J}$) when calculating the resulting object's angular acceleration (Lamb 1924; Brennen 1982).

For objects moving in unsteady flows with non-negligible viscous effects, in addition to the added mass (moment of inertia), the vorticity generated on the body surface and its subsequent diffusion and advection into the surrounding flow could also be important (Howe 1995). To understand whether the added-mass coefficient will deviate from the potential flow calculation due to the viscous effect, extensive investigations have been attempted to quantify the C_A of a spherical solid particle (Mei, Lawrence & Adrian 1991) and bubble (Mei & Klausner 1992) in flows with small-amplitude oscillations, as well as a rigid spherical particle in an oscillatory (Chang & Maxey 1994) and constantly accelerated flow (Chang & Maxey 1995). These results all indicated that the added-mass coefficient (C_A) of a sphere is 0.5, independent of the particle Reynolds number, Strouhal number and, more importantly, the slip (clean gas bubbles) and no-slip (rigid spheres) boundary conditions. Note that finding that the added-mass force is independent of the object surface boundary condition allows separating the hydrodynamic effects due to vorticity from those described by the irrotational flow theory. The added-mass coefficient of objects with arbitrary shapes calculated from the irrotational potential flow theory (Lamb 1924) can therefore be directly applied to bubbles moving in turbulence with finite Reynolds numbers.

After separating the added-mass force from other hydrodynamic forces that may depend on the particle Reynolds number, the equation of particle motion, including both the translational and rotational components, can be expressed following the generalized Kelvin–Kirchhoff equations (Lamb 1924; Howe 1995),

$$(m_b \boldsymbol{I} + \boldsymbol{A})\boldsymbol{a}_s + \boldsymbol{\Omega} \times ((m_b \boldsymbol{I} + \boldsymbol{A})\boldsymbol{u}_s) = \boldsymbol{F} + (m_b - \rho_l V_b)\boldsymbol{g}, \tag{1.1a}$$

$$(\boldsymbol{J} + \boldsymbol{D})\boldsymbol{a}_s + \boldsymbol{\Omega} \times ((\boldsymbol{J} + \boldsymbol{D})\boldsymbol{\Omega}) + \boldsymbol{u}_s \times (\boldsymbol{A}\boldsymbol{u}_s) = \boldsymbol{\Gamma}, \tag{1.1b}$$

where $\boldsymbol{\Omega}$ is the instantaneous angular velocity of the bubble, $\boldsymbol{I}$ and $\boldsymbol{J}$ are the unit tensor and inertia tensor of the object, respectively. Here $\boldsymbol{F}$ and $\boldsymbol{\Gamma}$ are the force and torque arising from the surrounding flow. For an oblate spheroid, the added-mass tensor $\boldsymbol{A}$ and added moment of inertia tensor $\boldsymbol{D}$ are diagonal if they are in the body-axis frame along the particle's axis of symmetry. The last term on the right-hand side of (1.1*a*) accounts for the buoyancy force with $\boldsymbol{g}$ being the gravitational constant. Here, (1.1*a*) and (1.1*b*) are fully coupled to determine the translational and rotational momentum balance of a particle. They have to be solved simultaneously along with the Navier–Stokes equation for the surrounding fluid to determine the bubble motion.

This framework can be used to understand the non-rectilinear path of a bubble rising in an otherwise quiescent medium (Mougin & Magnaudet 2006; Cano-Lozano *et al.* 2016; Mathai, Lohse & Sun 2020). A finite-sized bubble rising in a fluid at rest typically begins with a straight vertical path which develops into a two-dimensional zigzag motion followed by a spiral circular trajectory. Such a non-rectilinear motion of bubbles results from the balance between the wake-induced hydrodynamic loads (forces and torques) and the added-mass effects (Fernandes *et al.* 2008). Mougin & Magnaudet (2006) utilized the generalized Kevin–Kirchhoff equation to extract the contributions of different forces acting on a freely rising spheroidal bubble with a fixed shape. The added-mass force is important for both zigzag and helix motions. During zigzag motions, the translational added-mass force along the vertical direction is approximately 13 % of the buoyancy force. For the helix motion, along the lateral direction, the centripetal added mass ($\boldsymbol{\Omega} \times (\boldsymbol{A}\boldsymbol{u}_s)$) balances the bubble acceleration in the direction normal to the bubble trajectory, while the transverse added-mass force opposes the sum of the bubble lateral velocity change and the buoyancy force projected to the lateral direction. These findings show that the added-mass force is essential to the non-rectilinear motion of bubbles rising in an otherwise quiescent aqueous medium.

Evaluating the added-mass force experimentally is quite challenging and it was often conducted with the assistance of simulation. De Vries, Luther & Lohse (2002) experimentally investigated an induced oscillation of a bubble, after being tripped by a wire, while rising in quiescent water. This work showed that, without the added-mass effects, the observed bubble path oscillations could not be reproduced through calculations. Furthermore, Lavrenteva, Prakash & Nir (2016) studied the interaction of air bubbles in low-Reynolds-number Taylor–Couette flows and demonstrated that the added-mass force is key to explaining the observed separation of neighbouring bubbles (Prakash *et al.* 2013).

Although these works clearly articulated the importance of the added-mass force for bubbles, it remains elusive how to prescribe a correct added-mass tensor for a deformable bubble subjected to intense turbulent acceleration where the deformation and bubble orientation are strongly coupled with the surrounding flow. In the current work, we intend to use simultaneous measurements of both bubbles and surrounding turbulence to constrain the added-mass tensor of deforming bubbles in intense turbulence. In § 2, we briefly introduce the experimental set-up and discuss the quantities needed to constrain the added-mass tensor $\boldsymbol{A}$ experimentally. The analytical solutions for rigid geometries such as spheres, spheroids and cylinders are discussed in appendix A, which are later used to verify whether they can be directly applied to determine the added-mass effects experienced by deformable bubbles, whose shapes and orientations are coupled with turbulence. The procedure to estimate the added mass, including a constant C_A (§ 3.2) and the full tensorial form $\boldsymbol{C}_A$ (§ 3.3) and how they depend on the bubble shape and orientation in turbulence is introduced in § 3. Section 4 summarizes the paper and presents suggestions for future research.

2. Experimental methods

2.1. *Experimental facility*

Experiments were conducted in a vertical, 2.7-metre-tall water tunnel named V-ONSET (Masuk *et al.* 2019*b*), which was specifically designed and built to study the interaction of deformable air bubbles with intense turbulence. Nearly homogeneous and isotropic turbulence (known as HIT) was maintained in this set-up via randomized high-speed jets with speeds reaching up to 12 m s^{-1}, which were driven by a pressurized water tank connected to a 3-D-printed device, i.e. the jet array. This array consists of 88 jet nozzles, each of which is controlled by a dedicated solenoid valve, and the array sits atop an octagonal test section with a shape designed to provide flat optical windows covering the tunnel's perimeter. The mean turbulence energy dissipation rate in the measurement section was approximately $\langle\epsilon\rangle = 0.5$ m^2 s^{-3}, with a Taylor-scale Reynolds number of $Re_\lambda = 346$.

Bubbles were injected from the bottom of the test section through a bubble bank consisting of four islands of capillary needles with two different sizes. Most bubbles in the test section were around 2–7 mm in diameter, with the majority around 3–4 mm. This bubble size roughly ranges from 40η to 140η (η is the Kolmogorov scale), which falls within the inertial range of turbulence. The injected bubbles slowly rise to the centre of the test section, where they encounter turbulence. To extend the residence time of bubbles in the interrogation volume, a downward mean flow was set at around 25 cm s^{-1} to slow the bubble rise velocity. Additional set-up details and turbulence characteristics can be found in Masuk *et al.* (2019*b*).

The data acquisition system consists of six high-speed cameras that can capture images at 4000 frames per second at their full resolution of one megapixel. These six cameras were strategically placed around the centre of the measurement section in order to optimize the three-dimensional reconstruction of the bubble geometry. Furthermore, the water phase was seeded with density-matched tracer particles in order to visualize the flows around bubbles. Each camera has a dedicated light panel that casts the shadows of bubbles and surrounding tracer particles onto the cameras' imaging plane, and the two phases were segmented from images based on their size and contrast. The silhouettes of bubbles from all six cameras were combined using a recently developed virtual-camera visual hull method (Masuk, Salibindla & Ni 2019*a*) to reconstruct their geometries. The tracer particles were processed through another in-house particle tracking code (Tan *et al.* 2019, 2020) to analyse a high concentration of tracer particles around each bubble. In total, we collected approximately 6942 bubble trajectories with 30–40 tracer particles surrounding each bubble. These data sets will be used to extract the statistics of the bubble acceleration and the added-mass force.

2.2. *Summary of measurable quantities*

This section summarizes the physical quantities measured through our experiments. Figure 1 shows an example bubble trajectory approximately 400 frames in length, where the reconstructed bubble geometries are plotted once every one hundred frames along the trajectory. The geometry can be used to acquire the bubble size (D), aspect ratio ($\chi = r_1/r_3$) and the orientation of both semi-major ($\hat{\boldsymbol{r}}_1$) and semi-minor ($\hat{\boldsymbol{r}}_3$) axes. Moreover, the three-dimensional locations of surface points on the reconstructed geometry can be averaged to obtain the centre of mass of the bubble, which was tracked over time to construct the bubble trajectory.

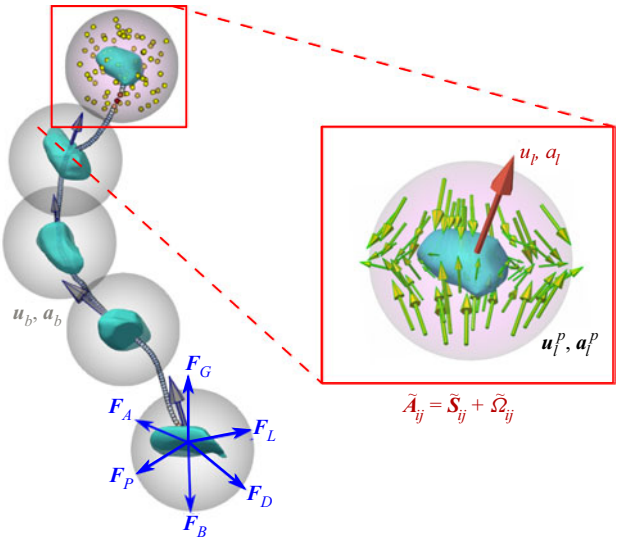

Figure 1. Reconstructed three-dimensional trajectory of a bubble ($D = 5.1$ mm) over 0.1 s (400 frames). The three dimensional (3-D) bubble geometries are shown every hundred frames as green blobs. The grey arrows protruding from the centre of these blobs represent the instantaneous bubble velocities. A sphere around each bubble represents a search volume that is used to seek tracer particles, whose locations for one time instant are marked as yellow dots. Their velocity $\boldsymbol{u}_l^p$ are indicated in the zoomed-in picture. The blue arrows on one bubble represent all the relevant forces experienced by the bubble.

To obtain the bubble velocity ($\boldsymbol{u}_b$) and acceleration ($\boldsymbol{a}_b$) along their trajectories, each bubble track is then convoluted with a Gaussian kernel (Mordant, Crawford & Bodenschatz 2004), which acts as a low-pass filter that reduces the positional uncertainties to allow accurately estimating velocity and acceleration. The acceleration standard deviation is sensitive to noise and the selected filter length, and we follow the procedure introduced by Voth *et al.* (2002) to justify the filter length used. In figure 2(*a*), the standard deviation of the bubble acceleration $\sqrt{\langle a_b^2 \rangle}$ in the horizontal (x) direction is shown as a function of the temporal filter width (τ) normalized by the Kolmogorov time scale, $\tau_\eta = 1.4$ ms. The initial sharp decay of $\sqrt{\langle a_b^2 \rangle}$ is due to the noise removal, while the later gradual change is due to the signal being smoothed. These results are consistent with previous findings (Voth *et al.* 2002; Ni, Huang & Xia 2012). A correct filter length can be obtained by fitting the data with a superposition of a power law and an exponential function to account for the fast and slow decays, respectively. The fit is shown as a solid line, while the contribution of the exponential term alone is shown as a dashed line. The vertical intercept of the dashed line at $\tau/\tau_\eta = 0$ provides the best estimate of the acceleration standard deviation. Based on this value, the filter length of $\tau/\tau_\eta = 0.58$ was consistently used to smooth the bubble trajectories.

The same procedure can be repeated to calculate the tracer velocity ($\boldsymbol{u}_l^p$) and acceleration ($\boldsymbol{a}_l^p$), where the superscript p represents individual tracer particles to distinguish them from the locally averaged fluid properties that will be introduced later. In figure 2(*a*), the same filter-length test has also been performed for tracer particles, and the results are very close to bubbles. Therefore, the same filter length was adopted for both phases. Finally, figure 2(*b*) shows the probability density functions (p.d.f.) for $\boldsymbol{a}_b$ and $\boldsymbol{a}_l^p$ in two different directions, which both exhibit a stretched exponential shape that is consistent with previous

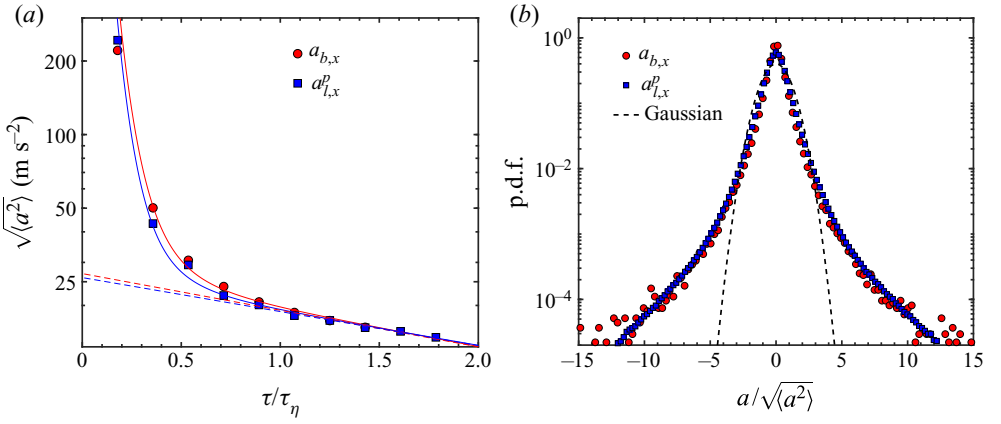

Figure 2. (*a*) The standard deviation of the bubble and flow acceleration versus the filter length. For a description of the solid lines and the dashed lines, please see the text below. (*b*) The distribution of the normalized bubble and tracer accelerations in the horizontal direction using a fixed filter width of $\tau = 0.58\tau_\eta$. The dashed line represents a Gaussian function with the same variance as the corresponding data.

works (Voth *et al.* 2002; Volk *et al.* 2008; Prakash *et al.* 2012). The acceleration p.d.f.s of both finite-sized bubbles and small tracer particles are surprisingly close to each other, which may be due to some competing effects. As shown by Qureshi *et al.* (2007) and Brown, Warhaft & Voth (2009), for finite-sized neutrally buoyant particles, although the acceleration p.d.f. shape changes little (except at tails Volk *et al.* (2011)) with finite size effects, the acceleration variance should decrease as the particle size increases. On the other hand, small microbubbles with a significant density difference but no finite-size effect seem to experience large acceleration variance in turbulence (Volk *et al.* 2008; Mathai *et al.* 2016). These two competing effects may neutralize each other, resulting in finite-sized bubbles and tracers sharing similar acceleration p.d.f.s.

Figure 1 illustrates that, at each time instant along a bubble trajectory, a search volume (grey semitransparent sphere) of radius $D_s/2$ ($D_s = 4D$, where D is the equivalent bubble diameter) is used to seek tracer particles with velocity $\boldsymbol{u}_l^p$ in the vicinity of a bubble with its centre of mass at location $\boldsymbol{x_0}$. Applying the Taylor expansion allows decomposition of the flow field within this range into leading terms: $\boldsymbol{u}_l(\boldsymbol{x_0})$ and $\tilde{A}_{ij}x_j^p$, where $\boldsymbol{u}_l = \sum_{p=1}^{n} \boldsymbol{u}_l^p(\boldsymbol{x_0} + \boldsymbol{x}^p)/N$ is the local mean flow averaged over N selected tracer particles. This procedure can be repeated to calculate the average flow acceleration $\boldsymbol{a}_l = \sum_{p=1}^{n} \boldsymbol{a}_l^p(\boldsymbol{x_0} + \boldsymbol{x}^p)/N$. Here $\tilde{A}_{ij}$ is the velocity gradient tensor around the bubble, and the tilde indicates that this gradient is coarse grained at the bubble size. The symmetrical component of $\tilde{A}_{ij}$ is the coarse-grained strain-rate tensor, $\tilde{S}_{ij}$. In addition, $\boldsymbol{x}^p$ is the separation vector directed from the bubble centre at $\boldsymbol{x_0}$ to the p^{th} tracer particle. Here $\tilde{A}_{ij}$ can be solved if there are four particles around a bubble. On average, 30–40 particles were used to perform least squares fits by seeking the minimum value of the squared residuals $\sum_p [u_i^p - \tilde{A}_{ij}x_j^p]^2$ (Pumir, Bodenschatz & Xu 2013; Ni *et al.* 2015). Several enforced criteria ensure that only the results with reliable $\tilde{A}_{ij}$ will be included in the statistics (Masuk, Salibindla & Ni 2020*b*). Due to the limited particle concentration, applying a search diameter of D_s tends to underestimate $\tilde{A}_{ij}$ around a bubble with size D due to the larger filter effect ($D_s > D$). Because both D_s and D fall in the inertial range, assuming a constant local energy dissipation rate enables correcting

$\tilde{A}_{ij}$ with a factor of $(D_s/D)^{2/3}$ to account for the scale difference. Additional details using different D_s to confirm this correction have been reported by Masuk *et al.* (2020*b*).

3. Results and discussion

3.1. *Governing equation*

To determine the motion of a deformable bubble in turbulence rigorously using the generalized Kelvin–Kirchhoff equation (1.1), the force ($\boldsymbol{F}$) and torque ($\boldsymbol{\Gamma}$) from the surrounding flow should be calculated by integrating the hydrodynamic stresses over the entire bubble surface at each time instant along its trajectory. This calculation remains impractical, however, due to the challenges of measuring the full three-dimensional flow velocity very close to the bubble surface at a sufficiently high resolution. Instead of directly measuring the total force, this paper expands the force on the right-hand side of (1.1*a*) by following the formulation provided by Magnaudet & Eames (2000) for spherical bubbles under the point-particle assumption, without considering the contribution of rotation. Furthermore, the original equation is adapted for deformable non-spherical bubbles by maintaining the tensorial form of the added-mass coefficient,

$$V_b\rho_b\frac{\mathrm{d}\boldsymbol{u}_b}{\mathrm{d}t} = \rho_l V_b \boldsymbol{C}_A\left(\frac{\mathrm{D}\boldsymbol{u}_l}{\mathrm{D}t} - \frac{\mathrm{d}\boldsymbol{u}_b}{\mathrm{d}t}\right) + \frac{\rho_l}{2}A_b C_D(\boldsymbol{u}_l-\boldsymbol{u}_b)|\boldsymbol{u}_l-\boldsymbol{u}_b| - V_b\nabla P_w + \boldsymbol{F}_h + \rho_l C_L(\boldsymbol{u}_l-\boldsymbol{u}_b)\times(\nabla\times\boldsymbol{u}_l) + V_b(\rho_l-\rho_b)g\hat{\boldsymbol{e}}_z, \tag{3.1}$$

where $\mathrm{d}/\mathrm{d}t$ and $\mathrm{D}/\mathrm{D}t$ represent the material derivative along the bubble and tracer Lagrangian trajectories, respectively. The five terms on the right-hand side of (3.1) represent the drag (F_D), pressure (F_P), history (F_h), lift (F_L) and the buoyancy (F_G) forces, respectively. Here, ∇P_w is the pressure gradient of flows around the bubble, $\boldsymbol{u}_l$ is the velocity of the unperturbed ambient flow taken at the centre of the bubble if the bubble were absent, and $\boldsymbol{u}_s = \boldsymbol{u}_b - \boldsymbol{u}_l$ is the bubble slip velocity. The equation also contains other constants, including the gravitational constant g and the density of water and gas, i.e. ρ_l and ρ_b. Here V_b is the bubble volume and A_b is the projected area of a volume-equivalent sphere. In addition, C_D and C_L are the drag and lift coefficients, respectively, and $\boldsymbol{C}_A$ is the added-mass coefficient tensor. In the previous work by Salibindla *et al.* (2020), the C_D and C_L for bubbles with contaminated interfaces in intense turbulent environments were determined based on the mean bubble and flow velocities, and they are

$$C_D = \max(24/Re_b(1+0.15Re_b^{0.687}), \min(f(Eo), f(Eo)/We^{1/3})), \tag{3.2}$$

$$C_L = \begin{cases} 2.671We^{3/5} & We < 0.1, \\ 1.25 - 1.608We^{3/5} & 0.1 < We < 0.9, \\ -0.23 & 0.9 < We, \end{cases} \tag{3.3}$$

where $f(Eo) = 8Eo/3(Eo+4)$ is a function of the Eötvös number, i.e. $Eo = (\rho_l - \rho_b)gD^2/\sigma$. The bubble Reynolds number and Weber number are defined as $Re_b = |u_b - u_l|D/\nu_l$ and $We = 2.13\rho(\epsilon D)^{2/3}D/\sigma$, respectively (2.13 is the Kolmogorov constant for the second-order longitudinal structure function). Here We determines the turbulence-induced deformation. The bubble size (D) was determined from the three-dimensional shape reconstruction for each time instant along a bubble trajectory, and instantaneous local flows and bubble velocity were used to calculate Re_b and We. The local Weber number is determined using $We = \rho(\widetilde{\lambda_3}D)^2D/\sigma$, where $\widetilde{\lambda_3}$ is the

smallest eigenvalue of the coarse-grained velocity gradient tensor ($\tilde{A}_{ij}$) calculated around each bubble. As shown in a previous work by Masuk *et al.* (2020*b*), this provides a reliable method to evaluate the instantaneous *We*. These dimensionless numbers were then substituted in (3.2) and (3.3) to determine the instantaneous drag and lift coefficients, respectively.

Equation (3.1) ignores the contribution from the bubble rotation. For a deformable bubble moving through water, two mechanisms enable bubbles to reorient: rotation or deformation. In a quiescent medium, bubbles can reorient via rotation driven by the unbalanced-wake-induced force. For finite-sized bubbles deforming in intense turbulence, the reorientation was found to be dominated by deformation along a different direction (Masuk *et al.* 2020*a*). Therefore, in accordance to this recent finding, the rotation of the bubble ($\boldsymbol{\Omega}$) throughout the rest of this paper is assumed to be zero. As a result, the hydrodynamic torque, the added moment of inertia and corresponding equation (1.1*b*) are ignored for simplification.

After replacing the slip acceleration and the added-mass tensor $\boldsymbol{A}$ with $\boldsymbol{a}_s = \mathrm{d}\boldsymbol{u}_b/\mathrm{d}t - \mathrm{D}\boldsymbol{u}_l/\mathrm{D}t$ and $\boldsymbol{A} = \rho_l V_b \boldsymbol{C}_A$, respectively, (3.1) can be rearranged to isolate the bubble acceleration, which yields

$$\frac{\mathrm{d}\boldsymbol{u}_b}{\mathrm{d}t} = [V_b(\rho_b \boldsymbol{I} + \boldsymbol{C}_A \rho_l)]^{-1} \cdot \left[\rho_l V_b \boldsymbol{C}_A \cdot \frac{\mathrm{D}\boldsymbol{u}_l}{\mathrm{D}t} + V_b(\rho_l - \rho_b) g \hat{\boldsymbol{e}}_z + \frac{\rho_l}{2} A_b C_D (\boldsymbol{u}_l - \boldsymbol{u}_b)|\boldsymbol{u}_l - \boldsymbol{u}_b| + \rho_l C_L (\boldsymbol{u}_l - \boldsymbol{u}_b) \times (\boldsymbol{\nabla} \times \boldsymbol{u}_l) - V_b \boldsymbol{\nabla} P_w \right], \quad (3.4)$$

where $[V_b(\rho_b \boldsymbol{I} + \boldsymbol{C}_A \rho_l)]^{-1}$ represents the inverse of the total mass tensor that includes both the actual mass $V_b \rho_b \boldsymbol{I}$ and the added mass tensor $V_b \boldsymbol{C}_A \rho_l$. Because the determinant of the total mass tensor is always non-zero, the tensor is invertible. The right-hand side of (3.4) essentially calculates the dot product of the inverse of the total mass tensor with the total hydrodynamic force (vector) applied on the bubble, which results in the bubble acceleration vector $\mathrm{d}\boldsymbol{u}_b/\mathrm{d}t$ matching the left-hand side. Within the total hydrodynamic force, we ignore the history forces acting on the bubble based on the previous works by Takagi & Matsumoto (1996) and Magnaudet & Eames (2000), who suggested that the effects of the history force are typically negligible for bubbles with a large-Re_b ($Re_b > 50$). For finite-sized bubbles considered in this paper, the Re_b ranges between 200–4000, significantly greater than 50. Therefore, the history force is negligible for bubbles considered in our studies. Most quantities on the right-hand side of (3.4) can be directly determined for any given bubble trajectory (an example is shown in figure 1), including the instantaneous velocities ($\boldsymbol{u}_b$, $\boldsymbol{u}_l$) and accelerations ($\boldsymbol{a}_b = \mathrm{d}\boldsymbol{u}_b/\mathrm{d}t$, $\boldsymbol{a}_l = \mathrm{D}\boldsymbol{u}_l/\mathrm{D}t$) of the bubbles and surrounding flow. The velocity gradients ($\boldsymbol{\nabla} \times \boldsymbol{u}_l$) can also be estimated based on the discussions in § 2.2. Instantaneous C_D and C_L can be calculated from (3.2) and (3.3), respectively, based on Re_b, *Eo* and *We* calculated from instantaneous bubble and flow information. As aforementioned in § 2.2, $\boldsymbol{u}_l$, $\boldsymbol{a}_l$ and $\boldsymbol{\nabla} \times \boldsymbol{u}_l$ can be determined using the velocities of several tracer particles located within a distance of two times the bubble diameter away from the centre of the bubble. If $\boldsymbol{C}_A$ is known, the entire right-hand side of (3.4) can be calculated for each bubble trajectory.

3.2. *Constant C_A*

Equation (3.4) provides a method to estimate the added-mass coefficient since both sides of the equation can be measured simultaneously and independently from the two phases,

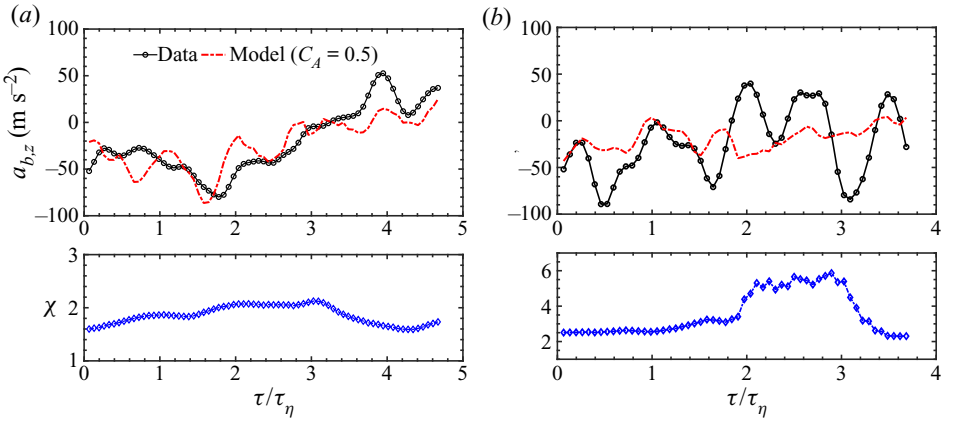

Figure 3. The time series of the vertical acceleration of (*a*) a weakly deformed bubble and (*b*) a strongly deformed bubble. In conjunction with the measured results, the time series of the bubble acceleration calculated from (3.4) using $C_A = 0.5$, accompanied by the aspect ratio time trace, is also shown.

one side from the bubble statistics and the other side from the flow statistics, with the only unknown being the added-mass coefficient. Because this equation should apply for bubbles of any shape, the first step is to test bubbles with weak deformation since their added-mass coefficient should be close to that of a sphere. The $\boldsymbol{C}_A$ for a spherical particle with three axes of symmetry can be simplified to a constant (C_A). Lamb (1924) (article 92) analytically solved the added-mass coefficient of a sphere accelerating through fluid following a rectilinear path and found that $C_A = 0.5$ in the direction of motion. This finding was followed by experiments (Sridhar & Katz 1995; Friedman & Katz 2002; Kendoush, Sulaymon & Mohammed 2007) and numerical simulations (Magnaudet 1997; Sankaranarayanan *et al.* 2002; Maliska & Paladino 2006), where the value of $C_A = 0.5$ was consistently reported or used in different flow conditions. This work can be used to examine whether our experiments produce consistent results with this expected value as the bubble shape approaches the spherical limit.

Figure 3 shows two example time traces of the bubble's vertical acceleration in conjunction with their respective aspect ratio. For both cases, the bubble acceleration measured from the bubble trajectory is shown as black circles, while the red dashed lines indicate the calculations based on the right-hand side of (3.4) by using $C_A = 0.5$. For the weakly deformed case (figure 3*a*), it is evident that the time trace of the calculated a_b is close to that of the measured results. This agreement suggests that, despite the non-negligible measurement uncertainties of the second-order quantities (e.g. velocity gradients and acceleration), this framework seems to successfully predict $\boldsymbol{a}_b$. The assumption of using the added mass coefficient close to 0.5 seems to be reasonable for bubbles close to the spherical shape. Furthermore, compared with the weakly deformed case, applying $C_A = 0.5$ seems to underpredict the acceleration fluctuations of the strongly deformed bubble, as shown in figure 3(*b*). This indicates that the acceleration fluctuation and added-mass coefficient may be coupled, and both may change as a function of the bubble deformation. Strictly speaking, (3.4) should only be applied to microbubbles with their sizes below the Kolmogorov scale immersed in a surrounding linear flow. Here, we assume that this equation may also work for finite-sized bubbles with their surrounding flow coarse-grained at the bubble size.

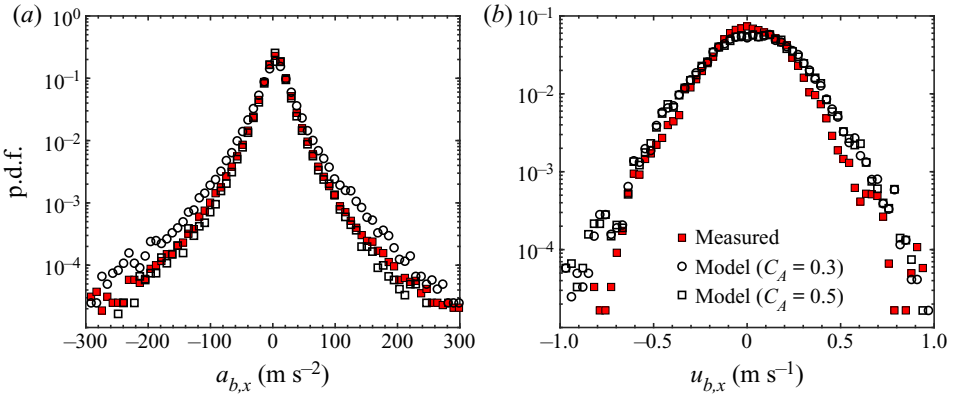

Figure 4. The distribution of (*a*) the horizontal bubble acceleration and (*b*) the horizontal bubble velocity, obtained from the measured data (red square) and calculated from (3.4) with two different C_A values of 0.3 (open circle) and 0.5 (open square).

Before discussing the dependence of C_A on the geometry of finite-sized deformable bubbles, we aim at identifying a statistical quantity that can be used to constrain C_A. Since C_A is closely related to the acceleration fluctuation, the p.d.f.s of one component of the calculated accelerations using two different values of C_A are shown in figure 4(*a*). For both C_A, the calculated p.d.f.s exhibit a stretched exponential form, which is consistent with our observations and other previous measurements of fluid acceleration in turbulence (Voth *et al.* 2002; Volk *et al.* 2008; Prakash *et al.* 2012). Applying $C_A = 0.5$ appears to produce a p.d.f. that agrees with the measured results. Since $C_A = 0.5$ was derived for rigid spherical particles, this agreement suggests that a large portion of our bubbles are not significantly deformed, which is consistent with the fact that 81 % of the bubbles have an aspect ratio smaller than $\chi = 2$. Despite the overall good agreement, some minor deviation is observed at the tails for large acceleration, which indicates that $C_A = 0.5$ may not work well for bubbles experiencing strong acceleration. This observation will be further discussed later in this section. Moreover, the p.d.f. calculated by employing a constant $C_A = 0.3$ seems to spread wider about the central value, thereby overpredicting the fluctuation of the bubble acceleration. This is expected since a smaller C_A suggests a reduced effective bubble inertia; under the same hydrodynamic forces, bubbles tend to experience greater acceleration.

The same calculation is repeated for the p.d.f. of the bubble velocity to examine its sensitivity to C_A. Like the acceleration, the bubble velocity can be determined from their trajectories or by integrating the calculated bubble acceleration from (3.4). The p.d.f.s of one component of the horizontal bubble velocity calculated from such an integration using both $C_A = 0.3$ and 0.5 are shown in figure 4(*b*). Both p.d.f.s agree with each other and the measured results, suggesting that the velocity p.d.f.s is less sensitive to the value of C_A. This is expected since many events with strong acceleration are probably smoothed during integration and thus not reflected in the velocity p.d.f.. Similar findings were also reported by Calzavarini *et al.* (2012) for neutrally buoyant finite-sized particles, which suggested that the acceleration statistics are dominated by the inertial effects while the velocity statistics are dominated by the drag and history effects.

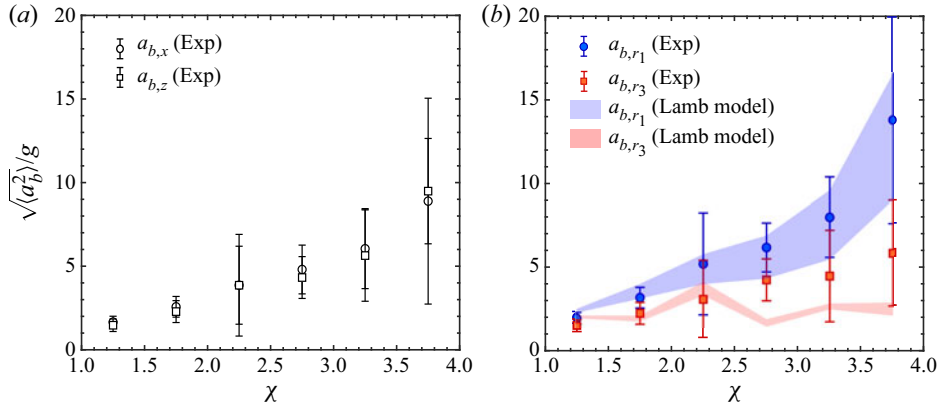

Figure 5. The standard deviation of the bubble acceleration along (*a*) the horizontal (x) and vertical (z) directions in the laboratory frame and (*b*) the semi-major ($\hat{\boldsymbol{r}}_1$) and semi-minor ($\hat{\boldsymbol{r}}_3$) in the bubble body-axis frame, normalized by the gravitational constant g, versus the bubble aspect ratio χ. The shaded areas in panel (*b*) represent the range of acceleration standard deviation calculated by assuming that the added-mass coefficient $\boldsymbol{C}_A$ follows the potential flow solutions either for prolates or oblates.

3.3. *Tensorial form of the added-mass coefficient*

Based on the previous tests, we conclude that C_A can be constrained by the acceleration variance. The $\sqrt{\langle a_b^2 \rangle}$ in both horizontal and vertical directions are shown in figure 5(*a*) as a function of the bubble aspect ratio χ, where χ represents the track-averaged bubble aspect ratio. The $\sqrt{\langle a_b^2 \rangle}$ of both directions increase from approximately $\sim 2g$ to $\sim 10g$. This large value of $\sqrt{\langle a_b^2 \rangle}$ can be attributed to the strong ambient turbulence around bubbles with an average energy dissipation rate of 0.5 $\mathrm{m}^2\ \mathrm{s}^{-3}$ (Masuk *et al.* 2019*b*). No significant difference in acceleration between the two directions is observed since the buoyancy effect is overwhelmed by the intense turbulence. The error bars in this figure were calculated by dividing the data set into six equal subsets and calculating $\sqrt{\langle a_b^2 \rangle}$ among these them, similar to the work by Voth (2000).

Despite establishing a connection between the standard deviation of acceleration with the added-mass coefficient, we have thus far been limited to a constant C_A, which only works for spherical particles. For deformable bubbles, the added-mass coefficient ($\boldsymbol{C}_A$) is a full 3×3 second-rank tensor, where each element must be determined.

To address this challenge, we examine (3.1) and (3.4), which are formulated using the added mass $\boldsymbol{A}$ and its coefficient $\boldsymbol{C}_A$ defined in the laboratory frame with three coordinates $(\hat{\boldsymbol{e}}_x, \hat{\boldsymbol{e}}_y, \hat{\boldsymbol{e}}_z)$. In a frame ($\mathcal{R}$) aligned with the body axes of the bubble $(\hat{\boldsymbol{r}}_1, \hat{\boldsymbol{r}}_2, \hat{\boldsymbol{r}}_3)$, the added-mass coefficient tensor can be denoted as ${\boldsymbol{C}_A}^{\mathcal{R}}$. When bubbles undergo only affine deformation, their shapes will remain spheroid with geometric symmetries. The ${\boldsymbol{C}_A}^{\mathcal{R}}$ can then be simplified into a diagonal matrix (Newman 1977), i.e. ${\boldsymbol{C}_A}^{\mathcal{R}} \equiv \mathrm{diag}(C_A^{r_1}, C_A^{r_2}, C_A^{r_3})$, with the superscripts (r_1, r_2, and r_3) denoting one of the three principal bubble axes. The two tensorial coefficients $\boldsymbol{C}_A$ and $\boldsymbol{C}_A^{\mathcal{R}}$ and their corresponding frames can be connected via a rotation matrix $\boldsymbol{R}$, following $\boldsymbol{C}_A = \boldsymbol{R}^T\, {\boldsymbol{C}_A}^{\mathcal{R}}\, \boldsymbol{R}$. Our experiments provided a full three dimensional (3-D) reconstruction of each bubble geometry, from which the bubble body-axis frame ($\mathcal{R}$) and the rotation matrix $\boldsymbol{R}$ at each time instant can be determined.

In the bubble body-axis frame, (3.4) can be explicitly written as three independent equations, linking each diagonal component of $\boldsymbol{C}_A^{\mathcal{R}}$, i.e. $C_A^{r_1}$, $C_A^{r_2}$, $C_A^{r_3}$, to the bubble acceleration along one of the three bubble principal axes, i.e. $a_{b,r_1}, a_{b,r_2}, a_{b,r_3}$, respectively. Because both the bubble acceleration ($\boldsymbol{a}_b$) and its principal axes ($\hat{\boldsymbol{r}}_i$, $i = 1, 2, 3$) can be determined using our measurements, the projected acceleration a_{b,r_i} can be easily calculated by using $\boldsymbol{a}_b \cdot \hat{\boldsymbol{r}}_i$ for every bubble at every instant, which enables obtaining the bubble standard deviation projected along the three bubble principal axes.

Figure 5(b) shows the bubble acceleration standard deviation projected along the bubble semi-major (a_{b,r_1}) and semi-minor axes (a_{b,r_3}), respectively. Although the standard deviations of a_x and a_z in the laboratory frame appear to be very close to each other for all bubble aspect ratios considered, $\sqrt{\langle a_{b,r_1}^2 \rangle}$ is systematically larger than $\sqrt{\langle a_{b,r_3}^2 \rangle}$, and their differences increase as χ grows. This difference brings confidence to our experiments, because if the bubble orientation is not well reconstructed, it is likely that the acceleration standard deviations along both bubble principal axes do not show any difference, as with what is shown in the laboratory coordinates along the x and z axes. In addition, because the added-mass coefficient along the major axis accompanied by a smaller frontal area (end-on configuration) should be smaller, the acceleration standard deviation should be larger, which is consistent with the trend observed in figure 5(b).

The standard deviation of each acceleration component can be used to constrain one respective component of $\boldsymbol{C}_A^{\mathcal{R}}$, for which purpose an iterative fit was put forward. Consider $C_A^{r_1}$ for example, where an initial guess of $C_A^{r_1} = 0.5$ was used. For each iteration, $C_A^{r_1}$ was updated by adding its value from the previous iteration with a small step. The acceleration standard deviation was then calculated from the right-hand side of (3.4) by replacing $\boldsymbol{C}_A$ with a constant of $C_A^{r_1}$ and projecting all other terms to the direction of $\hat{\boldsymbol{r}}_1$, and the resulting acceleration was naturally in the direction of $\hat{\boldsymbol{r}}_1$. The total squared difference between the calculated acceleration standard deviation and those measured directly from bubble trajectories was used to correct $C_A^{r_1}$. The iteration continued until the difference using the two independent methods ceased decreasing, and the same procedure was repeated for each bubble aspect ratio χ. For each χ, in addition to the mean value, the uncertainty of C_A is estimated by repeating the same iterative fit to the upper and lower bounds of $\sqrt{\langle a_{b,r_1}^2 \rangle}$ in figure 5(b).

The calculated $C_A^{r_1}$ is shown as closed circles with error bars in figure 6. In the limit of spherical and isolated bubbles, C_A should be equal to 0.5. Although C_A seems to have a trend of getting close to 0.5 as χ approaches one, it is slightly larger than 0.5 at $\chi = 1.25$. One explanation for such a result is that bubbles in our experiments are not isolated; the bubble volume concentration (ϕ) is kept close to 2 %, striking a balance between acquiring sufficient data within an affordable period and possible contamination due to bubble–bubble interaction. At this concentration, it has been shown that the bubble–bubble interaction could entail non-negligible effects on C_A with the largest reported value close to $C_A = 1$ at $\phi = 2$ % by Pudasaini (2019) and the smallest value close to $C_A = 0.6$ by Sankaranarayanan *et al.* (2002).

In addition, C_A seems to gradually decrease as χ increases, and we seek solutions from Lamb's potential flow models to understand this trend. Applying these models, however, requires knowing whether the shape of deformed bubbles in turbulence follows prolate or oblate spheroids as well as along which direction they are accelerating. Prolate and oblate spheroids represent ideal approximations at extremes, but a typical deformed bubble is shaped somewhere in-between. If a criterion of r_2 smaller or larger than $(r_1 + r_3)/2$ is

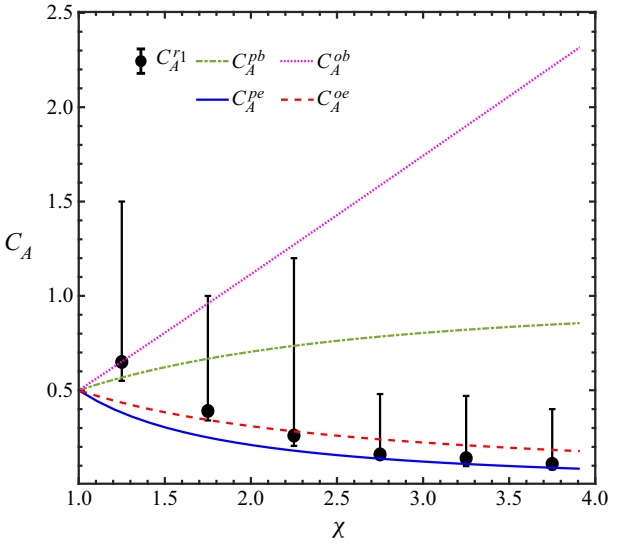

Figure 6. The added-mass coefficient tensor $\boldsymbol{C}_A$ versus the bubble aspect ratio χ. Symbols represent one diagonal element of $\boldsymbol{C}_A$ along the bubble semi-major axis. Four lines indicate different elements of $\boldsymbol{C}_A$ calculated based on the Lamb's model for prolates or oblates.

used to separate prolate from oblate bubbles in our results, approximately 59 % bubbles are close to prolate spheroids, slightly higher than the remaining 41 % oblate-like bubbles.

Figure 6 shows four lines calculated using the Lamb's potential flow model for prolate and oblate spheroids accelerating either end-on (along $\hat{\boldsymbol{r}}_1$) or broadside-on (along $\hat{\boldsymbol{r}}_3$) ((A 1) in appendix A). All four lines begin from $C_A = 0.5$ when $\chi = 1$, as expected. For either prolate or oblate spheroids accelerating end-on, C_A reduces systematically as χ increases. In this case, an increasing χ is equivalent to a reducing frontal area as spheroids accelerate through fluid, which results in a smaller volume of fluid that needs to be accelerated and hence a smaller C_A. The same principle also applies to the opposite limit, where spheroids accelerate broadside-on. In this case, as χ becomes larger, C_A increases along with the frontal area. In addition, C_A of oblate spheroids increases more sharply compared with that of prolate spheroids due to the difference in their broadside-projected areas. For C_A^{r1}, only two lines for the end-on configurations are relevant. It is evident that the acquired C_A^{r1}, constrained by $\sqrt{\langle a_{b,r_1}^2 \rangle}$, agrees with these two lines. This implies that the potential flow solution can accurately calculate the added mass coefficient, even for deformable bubbles, at least for those accelerating end-on.

We notice that the error bars of C_A^{r1} are not symmetric around the mean, unlike those for the measured $\sqrt{\langle a_{b,r_1}^2 \rangle}$, because C_A^{r1} is inversely proportional to the bubble standard deviation. When the lower limit of acceleration standard deviation approaches zero, the estimated C_A^{r1} moves closer to infinity. The same argument applies also to the other two components of the added mass tensor, C_A^{r2} and C_A^{r3}. Although both of them can be determined following the same procedure for C_A^{r1}, their acceleration standard deviations are so small that any small errors translate to large error bars in the plot of C_A. In fact, the error bars of C_A^{r3}, especially for large χ, are so large that they cover almost the entire figure. Instead of showing them in figure 6, we decided to compare them with the Lamb's model prediction using the acceleration standard deviation in figure 5(*b*).

Applying Lamb's model to the right-hand side of (3.4) requires us to classify bubbles into prolate or oblate spheroids. To simplify the problem, we assume all bubbles are either prolate ($\boldsymbol{C_A}^{\mathcal{R}} \equiv \mathrm{diag}(C_A^{pe}, C_A^{pb}, C_A^{pb})$) or oblate ($\boldsymbol{C_A}^{\mathcal{R}} \equiv \mathrm{diag}(C_A^{oe}, C_A^{oe}, C_A^{ob})$), and the exact formulations of three diagonal values can be found in appendix A. The calculated acceleration standard deviations along $\hat{\boldsymbol{r}}_1$ and $\hat{\boldsymbol{r}}_3$ are shown as the two shaded areas in figure 5(*b*) with the upper bounds of both areas showing results from all-prolate calculations and the lower bounds indicating results from all-oblate calculations.

It is clear that the measured acceleration standard deviation along $\hat{\boldsymbol{r}}_1$ falls right in the middle of the shaded area, confirming that the measured results agree with the potential flow calculation. But the measured $\sqrt{\langle a_{b,r_3}^2 \rangle}$ seems to be higher than the predicted one from the potential flow theory for large aspect ratios, $\chi > 2.25$. One possible explanation is that bubbles will experience necking when they undergo large deformation, which cause the geometry to deviate away from spheroids by having a small broadside projected area. As a result, the acceleration standard deviation along the bubble semi-minor axis may become slightly larger than the one predicted by the potential flow theory assuming spheroidal bubble shapes. In addition, we cannot completely rule out the possibility that bubbles with larger aspect ratios may be under the influence of rotation based on (1.1). This could be another reason for the observed difference between the measured and calculated $\sqrt{\langle a_{b,r_3}^2 \rangle}$ at large χ.

Finally, in addition to $\boldsymbol{C_A}$, the added-mass force is also sensitive to the relative orientation between the slip acceleration ($\boldsymbol{a_s}$) with the bubble principal axes, because this relative orientation determines if the bubble is preferentially accelerating end-on or broadside-on and the final magnitude of the added-mass force. Figure 7 shows the p.d.f. of the alignment between the bubble semi-major axis ($\boldsymbol{r}_1$) and slip acceleration ($\boldsymbol{a_s}$), i.e. $\langle \hat{\boldsymbol{a}}_s \cdot \hat{\boldsymbol{r}}_1 \rangle$, for four different aspect ratios. If their orientations are completely random, the p.d.f. of the dot product of the two unit vectors should follow a uniform distribution. A peak at around zero would suggest a perpendicular orientation, whereas a peak close to one would indicate an alignment between the two unit vectors. It can be seen that, in figure 7, a consistent preferential alignment between the bubble semi-major axis with the slip acceleration is observed for all aspect ratios considered, suggesting that bubbles prefer to accelerate along their semi-major axis (end-on). Moreover, such a preference seems to increase with χ as strongly deformed bubbles align better with the slip acceleration. Since an end-on configuration implies a smaller added-mass coefficient and larger acceleration fluctuation, this preferential alignment explains why the acceleration standard deviation along both horizontal and vertical directions in the laboratory frame increases as a function of the bubble aspect ratio.

It is surprising to find that the preferential alignment seems to be opposite to what has been observed for bubbles rising in an otherwise quiescent medium, in which the bubble semi-minor axis, instead of semi-major axis, is preferentially aligned with the slip acceleration direction (Magnaudet & Eames 2000). This difference can be attributed to the relationships among bubble deformable geometry, slip velocity, turbulent strains and slip acceleration. Note that bubble deformation is not determined by the added mass force; instead, it is driven by the gradient of dynamic pressure acting on its interface, including the contribution of both the slip velocity and turbulent strains. As a result, the bubble semi-minor axis shows preferential alignment with the slip velocity direction in both a quiescent and a turbulent aqueous medium. It just happens that the slip velocity and slip acceleration align with each other in a quiescent medium, which is not the

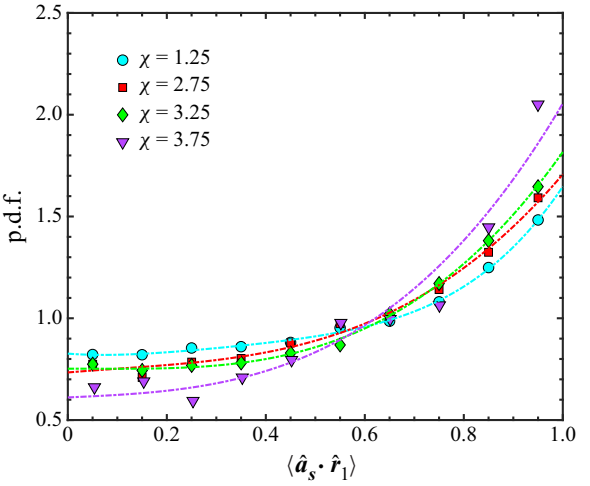

Figure 7. Probability density function of the cosine of the angle between the bubble semi-major axis ($\hat{\boldsymbol{r}}_1$) and the slip acceleration ($\hat{\boldsymbol{a}}_s$) for bubbles with different aspect ratios χ.

case in turbulence. In turbulence, as bubbles are deformed and elongated along its major axis, the acceleration along its major axis tends to increase, which dominates the slip acceleration. This explains the observed preferential alignment between the slip acceleration and the bubble semi-major axis.

4. Summary

Bubbles in turbulence are subjected to multiple hydrodynamic forces that are sensitive to the bubble geometry. Among them, the unsteady forces, such as the added-mass force, have received very little attention due to the technical challenges in reliably extracting them through experiments, despite their potential importance in turbulent multiphase flows. To address this problem, we developed an experimental framework combining a vertical water tunnel that produces intense turbulence with a diagnostic system that can simultaneously measure gas bubbles and their surrounding turbulence in 3-D.

The lift and drag coefficients in the governing equation of motion for bubbles were determined from the bubbles' velocity and surrounding flow for different Reynolds numbers and Weber numbers by Salibindla *et al.* (2020). Using these two coefficients, the instantaneous acceleration of bubbles can be estimated from the surrounding flow velocity and velocity gradients coarse-grained at the bubble size. The bubble acceleration can also be directly extracted using the bubble trajectories. These two independent estimations of the bubble acceleration enable constraining the added mass coefficient. Reliably extracting the added-mass coefficient requires accurately measuring the turbulent velocity gradients, acceleration of both phases and bubble reconstructed shapes in 3-D, which has really pushed the 3-D flow measurements to the extreme.

The added-mass coefficient is a 3×3 tensor, which becomes a diagonal tensor with only three unknown elements in the bubble body-axis frame. By projecting the entire equation of motion onto the bubble principal axes, each diagonal element in the added mass coefficient tensor can be uniquely linked to the standard deviation of the bubble acceleration along each respective bubble axis, which can be measured through our experiments with access to both bubble acceleration and their 3-D shapes. The acceleration

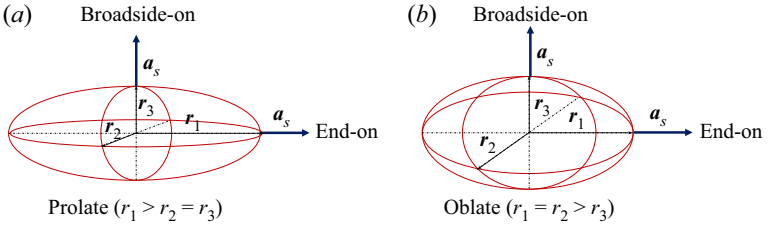

Figure 8. Schematics of four configurations of accelerating spheroids with known analytical solutions of C_A, including (*a*) a prolate spheroid and (*b*) an oblate spheroid, accelerating along their semi-minor ($\boldsymbol{r}_3$) axis (broadside-on) or semi-major ($\boldsymbol{r}_1$) axis (end-on).

standard deviation along the bubble semi-major axis increases with the bubble aspect ratio χ. This shows that the added-mass coefficient along the bubble semi-major axis for all values of χ can be determined, which seems to gradually decrease as χ increases. The acquired dependence agrees with the prediction from the potential flow theory for spheroids with the same aspect ratio accelerating end-on. This agreement can also be extended to other axes, such as the bubble minor axis, although less accurately due to the potential necking effect.

An additional finding is that deformed bubbles preferentially accelerate along their semi-major axis, and this preference seems to increase with the bubble aspect ratio, which suggests that bubbles tend to accelerate in turbulence end-on. This configuration results in a smaller frontal area and less fluid volume being accelerated, which in turns increases the bubble acceleration standard deviation. This explains why the observed bubble acceleration standard deviation in both vertical and horizontal axes in the laboratory frame rises as a function of χ.

Acknowledgements. We acknowledge the financial support from the National Science Foundation under the award numbers: 1854475 and CAREER-1905103.

Declaration of interests. The authors report no conflict of interest.

Author ORCIDs.
Rui Ni https://orcid.org/0000-0002-7178-1479.

Appendix A. Analytical solutions of the added-mass coefficient

Although the analytical solutions are available for both added mass and added moment of inertia tensors, here we only consider the added-mass tensor as the bubble rotation is ignored. A spheroid (oblate or prolate) or a cylinder is the simplest geometry to consider after a sphere. A potential flow solution for a cylinder accelerating perpendicular to its long axis shows that the added mass is equal to the mass of the fluid displaced by the cylinder (Brennen 1982), i.e. $C_A = 1$. Furthermore, extensive work has also been conducted to analyse the dependence of added mass for a cylinder under oscillating flows to understand the effect of vortex shedding on C_A (Sarpkaya 1975). In addition to a cylinder, Lamb (1924) analytically solved $\boldsymbol{C}_A$ for both a prolate spheroid and an oblate spheroid in articles 114 and 373 of his book, respectively. For such geometries, $\boldsymbol{C}_A$ was found to be a function of the object aspect ratio and whether the spheroid particle is accelerating along its semi-major ($\boldsymbol{r}_1$) axis (end-on) or its semi-minor ($\boldsymbol{r}_3$) axis (broadside-on). Figure 8 illustrates a prolate spheroid and an oblate spheroid moving end-on or broadside-on. The analytical solutions

for these four cases: prolate end-on (pe), prolate broadside-on (pb), oblate end-on (oe) and oblate broadside-on (ob) are given as

$$C_A^{pe} = \alpha_1/(2-\alpha_1); \quad C_A^{pb} = \beta_1/(2-\beta_1); \quad C_A^{oe} = \alpha_2/(2-\alpha_2); \quad C_A^{ob} = \beta_2/(2-\beta_2), \tag{A1a–d}$$

where, $\alpha_1 = (1-e^2)/e^3(\ln((1+e)/(1-e)) - 2e)$, $\beta_1 = (1-e^2)/e^3(e/(1-e^2) - 1/2\ln((1+e)/(1-e)))$, $\alpha_2 = 2/e^3(e - \sqrt{1-e^2}\sin^{-1}e)$, $\beta_2 = 1/e^3(\sqrt{1-e^2}\sin^{-1}e - e(1-e^2))$. Parameter $e = \sqrt{1-1/\chi^2}$ is the eccentricity of an object along its meridian and $\chi = r_1/r_3$ is the object aspect ratio.

References

Alméras, E., Mathai, V., Sun, C. & Lohse, D. 2019 Mixing induced by a bubble swarm rising through incident turbulence. *Intl J. Multiphase Flow* **114**, 316–322.

Batchelor, C.K. 1967 *An Introduction to Fluid Dynamics*. Cambridge University Press.

Brennen, C.E. 1982 A review of added mass and fluid inertial forces. *Tech. Rep.* CR 82.010. Brennen (CE), Sierra Madre, CA.

Brown, R.D., Warhaft, Z. & Voth, G.A. 2009 Acceleration statistics of neutrally buoyant spherical particles in intense turbulence. *Phys. Rev. Lett.* **103** (19), 194501.

Calzavarini, E., Volk, R., Lévêque, E., Pinton, J.-F. & Toschi, F. 2012 Impact of trailing wake drag on the statistical properties and dynamics of finite-sized particle in turbulence. *Physica* D **241** (3), 237–244.

Cano-Lozano, J.C., Martinez-Bazan, C., Magnaudet, J. & Tchoufag, J. 2016 Paths and wakes of deformable nearly spheroidal rising bubbles close to the transition to path instability. *Phys. Rev. Fluids* **1** (5), 053604.

Chang, E.J. & Maxey, M.R. 1994 Unsteady flow about a sphere at low to moderate Reynolds number. Part 1. Oscillatory motion. *J. Fluid Mech.* **277**, 347–379.

Chang, E.J. & Maxey, M.R. 1995 Unsteady flow about a sphere at low to moderate Reynolds number. Part 2. Accelerated motion. *J. Fluid Mech.* **303**, 133–153.

De Vries, J., Luther, S. & Lohse, D. 2002 Induced bubble shape oscillations and their impact on the rise velocity. *Eur. Phys. J.* B **29** (3), 503–509.

Deane, G.B. & Stokes, M.D. 2002 Scale dependence of bubble creation mechanisms in breaking waves. *Nature* **418** (6900), 839–844.

Du Cluzeau, A., Bois, G. & Toutant, A. 2019 Analysis and modelling of Reynolds stresses in turbulent bubbly up-flows from direct numerical simulations. *J. Fluid Mech.* **866**, 132–168.

Fernandes, P.C., Ern, P., Risso, F. & Magnaudet, J. 2008 Dynamics of axisymmetric bodies rising along a zigzag path. *J. Fluid Mech.* **606**, 209–223.

Friedman, P.D. & Katz, J. 2002 Mean rise rate of droplets in isotropic turbulence. *Phys. Fluids* **14** (9), 3059–3073.

Howe, M.S. 1995 On the force and moment on a body in an incompressible fluid, with application to rigid bodies and bubbles at high and low reynolds numbers. *Q. J. Mech. Appl. Maths* **48** (3), 401–426.

Jakobsen, H.A. 2008 Chemical reactor modeling. *Multiphase Reactive Flows*.

Kendoush, A.A., Sulaymon, A.H. & Mohammed, S.A.M. 2007 Experimental evaluation of the virtual mass of two solid spheres accelerating in fluids. *Exp. Therm. Fluid Sci.* **31** (7), 813–823.

Lamb, H. 1924 *Hydrodynamics*. University Press.

Lavrenteva, O., Prakash, J. & Nir, A. 2016 Effect of added mass on the interaction of bubbles in a low-Reynolds-number shear flow. *Phys. Rev.* E **93** (2), 023105.

Loisy, A. & Naso, A. 2017 Interaction between a large buoyant bubble and turbulence. *Phys. Rev. Fluids* **2** (1), 014606.

Magnaudet, J. 1997 The forces acting on bubbles and rigid particles. In *ASME Fluids Engineering Division Summer Meeting, FEDSM*, vol. 97, pp. 22–26.

Magnaudet, J. & Eames, I. 2000 The motion of high-Reynolds-number bubbles in inhomogeneous flows. *Annu. Rev. Fluid Mech.* **32** (1), 659–708.

Maliska, C.R. & Paladino, E.E. 2006 The role of virtual mass, lift and wall lubrication forces in accelerated bubbly flows. *Energy: Production, Distribution Conservation-Milan* **2006**, 953–962.

MASUK, A.U.M., QI, Y., SALIBINDLA, A.K.R. & NI, R. 2020*a* A phenomenological model on the deformation and orientation dynamics of finite-sized bubbles in both quiescent and turbulent media. *J. Fluid Mech.* (submitted).

MASUK, A.U.M., SALIBINDLA, A.K.R. & NI, R. 2019*a* A robust virtual-camera 3D shape reconstruction of deforming bubbles/droplets with additional physical constraints. *Intl J. Multiphase Flow* **120**, 103088.

MASUK, A.U.M., SALIBINDLA, A.K.R. & NI, R. 2020*b* Simultaneous measurements of deforming Hinze-scale bubbles with surrounding turbulence. *J. Fluid Mech.* **910**, A21.

MASUK, A.U.M., SALIBINDLA, A.K.R., TAN, S. & NI, R. 2019*b* V-ONSET (vertical octagonal noncorrosive stirred energetic turbulence): a vertical water tunnel with a large energy dissipation rate to study bubble/droplet deformation and breakup in strong turbulence. *Rev. Sci. Instrum.* **90** (8), 085105.

MATHAI, V., CALZAVARINI, E., BRONS, J., SUN, C. & LOHSE, D. 2016 Microbubbles and microparticles are not faithful tracers of turbulent acceleration. *Phys. Rev. Lett.* **117** (2), 024501.

MATHAI, V., LOHSE, D. & SUN, C. 2020 Bubble and buoyant particle laden turbulent flows. *Annu. Rev. Condens. Matter Phys.* **11**, 529–559.

MEI, R. & KLAUSNER, J.F. 1992 Unsteady force on a spherical bubble at finite Reynolds number with small fluctuations in the free-stream velocity. *Phys. Fluids* A **4** (1), 63–70.

MEI, R., LAWRENCE, C.J. & ADRIAN, R.J. 1991 Unsteady drag on a sphere at finite Reynolds number with small fluctuations in the free-stream velocity. *J. Fluid Mech.* **233**, 613–631.

MICHIYOSHI, I. & SERIZAWA, A. 1986 Turbulence in two-phase bubbly flow. *Nucl. Engng Des.* **95**, 253–267.

MORDANT, N., CRAWFORD, A.M. & BODENSCHATZ, E. 2004 Experimental lagrangian acceleration probability density function measurement. *Physica* D **193** (1–4), 245–251.

MOUGIN, G. & MAGNAUDET, J. 2006 Wake-induced forces and torques on a zigzagging/spiralling bubble. *J. Fluid Mech.* **567**, 185–194.

NEWMAN, J.N. 1977 *Marine Hydrodynamics*. Massachusetts Institute of Technology.

NI, R., HUANG, S.-D. & XIA, K.-Q. 2012 Lagrangian acceleration measurements in convective thermal turbulence. *J. Fluid Mech.* **692**, 395–419.

NI, R., KRAMEL, S., OUELLETTE, N.T. & VOTH, G.A. 2015 Measurements of the coupling between the tumbling of rods and the velocity gradient tensor in turbulence. *J. Fluid Mech.* **766**, 202–225.

PRAKASH, J., LAVRENTEVA, O.M., BYK, L. & NIR, A. 2013 Interaction of equal-size bubbles in shear flow. *Phys. Rev.* E **87** (4), 043002.

PRAKASH, V.N., TAGAWA, Y., CALZAVARINI, E., MERCADO, J., TOSCHI, F., LOHSE, D. & SUN, C. 2012 How gravity and size affect the acceleration statistics of bubbles in turbulence. *New J. Phys.* **14** (10), 105017.

PUDASAINI, S.P. 2019 A fully analytical model for virtual mass force in mixture flows. *Intl J. Multiphase Flow* **113**, 142–152.

PUMIR, A., BODENSCHATZ, E. & XU, H. 2013 Tetrahedron deformation and alignment of perceived vorticity and strain in a turbulent flow. *Phys. Fluids* **25** (3), 035101.

QURESHI, N.M., BOURGOIN, M., BAUDET, C., CARTELLIER, A. & GAGNE, Y. 2007 Turbulent transport of material particles: an experimental study of finite size effects. *Phys. Rev. Lett.* **99** (18), 184502.

SALIBINDLA, A.K.R., MASUK, A.U.M., TAN, S. & NI, R. 2020 Lift and drag coefficients of deformable bubbles in intense turbulence determined from bubble rise velocity. *J. Fluid Mech.* **894**, A20.

SANKARANARAYANAN, K., SHAN, X., KEVREKIDIS, I.G. & SUNDARESAN, S. 2002 Analysis of drag and virtual mass forces in bubbly suspensions using an implicit formulation of the lattice Boltzmann method. *J. Fluid Mech.* **452**, 61–96.

SARPKAYA, T. 1975 Forces on cylinders and spheres in a sinusoidally oscillating fluid. *J. Appl. Mech.* **42** (1), 32–37.

SRIDHAR, G. & KATZ, J. 1995 Drag and lift forces on microscopic bubbles entrained by a vortex. *Phys. Fluids* **7** (2), 389–399.

TAKAGI, S. & MATSUMOTO, Y. 1996 Force acting on a rising bubble in a quiescent liquid. *Trans. ASME: Fluids Engng Div.* **236**, 575–580.

TAN, S., SALIBINDLA, A.K.R., MASUK, A.U.M. & NI, R. 2019 An open-source Shake-the-Box method and its performance evaluation. In *13th International Symposium on Particle Image Velocimetry – ISPIV 2019*.

TAN, S., SALIBINDLA, A.K.R., MASUK, A.U.M. & NI, R. 2020 Introducing openLPT: new method of removing ghost particles and high-concentration particle shadow tracking. *Exp. Fluids* **61** (2), 47.

VERSCHOOF, R.A., VAN DER VEEN, R.C.A., SUN, C. & LOHSE, D. 2016 Bubble drag reduction requires large bubbles. *Phys. Rev. Lett.* **117** (10), 104502.

VOLK, R., CALZAVARINI, E., LEVEQUE, E. & PINTON, J.-F. 2011 Dynamics of inertial particles in a turbulent von Kármán flow. *J. Fluid Mech.* **668**, 223–235.

VOLK, R., CALZAVARINI, E., VERHILLE, G., LOHSE, D., MORDANT, N., PINTON, J.-F. & TOSCHI, F. 2008 Acceleration of heavy and light particles in turbulence: comparison between experiments and direct numerical simulations. *Physica* D **237** (14–17), 2084–2089.

VOTH, G.A. 2000 *Lagrangian Acceleration Measurements in Turbulence at Large Reynolds Numbers*. Cornell University.

VOTH, G.A., LA PORTA, A., CRAWFORD, A.M., ALEXANDER, J. & BODENSCHATZ, E. 2002 Measurement of particle accelerations in fully developed turbulence. *J. Fluid Mech.* **469**, 121–160.

YU, X., HENDRICKSON, K. & YUE, D.K.P. 2020 Scale separation and dependence of entrainment bubble-size distribution in free-surface turbulence. *J. Fluid Mech.* **885**, R2.